

Article

# Quantum Circuits for the Preparation of Spin Eigenfunctions on Quantum Computers

Alessandro Carbone <sup>1,2</sup>, Davide Emilio Galli <sup>2</sup> , Mario Motta <sup>3,\*</sup> and Barbara Jones <sup>3</sup>

<sup>1</sup> Theory and Simulation of Materials (THEOS), National Centre for Computational Design and Discovery of Novel Materials (MARVEL), École Polytechnique Fédérale de Lausanne, 1015 Lausanne, Switzerland; alessandro.carbone@epfl.ch

<sup>2</sup> Dipartimento di Fisica, Università degli Studi di Milano, Via Celoria 16, 20133 Milano, Italy; davide.galli@unimi.it

<sup>3</sup> IBM Quantum, IBM Research Almaden, 650 Harry Road, San Jose, CA 95120, USA; bajones@us.ibm.com

\* Correspondence: mario.motta@ibm.com

**Abstract:** The application of quantum algorithms to the study of many-particle quantum systems requires the ability to prepare wave functions that are relevant in the behavior of the system under study. Hamiltonian symmetries are important instruments used to classify relevant many-particle wave functions and to improve the efficiency of numerical simulations. In this work, quantum circuits for the exact and approximate preparation of total spin eigenfunctions on quantum computers are presented. Two different strategies are discussed and compared: exact recursive construction of total spin eigenfunctions based on the addition theorem of angular momentum, and heuristic approximation of total spin eigenfunctions based on the variational optimization of a suitable cost function. The construction of these quantum circuits is illustrated in detail, and the preparation of total spin eigenfunctions is demonstrated on IBM quantum devices, focusing on three- and five-spin systems on graphs with triangle connectivity.



check for updates

**Citation:** Carbone, A.; Galli, D.E.; Motta, M.; Jones, B. Quantum Circuits for the Preparation of Spin Eigenfunctions on Quantum Computers. *Symmetry* **2022**, *14*, 624. <https://doi.org/10.3390/sym14030624>

Academic Editor: Jim Freericks

Received: 10 March 2022

Accepted: 17 March 2022

Published: 21 March 2022

**Publisher's Note:** MDPI stays neutral with regard to jurisdictional claims in published maps and institutional affiliations.



**Copyright:** © 2022 by the authors. Licensee MDPI, Basel, Switzerland. This article is an open access article distributed under the terms and conditions of the Creative Commons Attribution (CC BY) license (<https://creativecommons.org/licenses/by/4.0/>).

**Keywords:** quantum computing; spin liquids; eigenstates; quantum error mitigation

## 1. Introduction

One of the central goals of quantum mechanics is to determine the behavior of multiple interacting particles. A fundamental and important example is the determination of the eigenstates of spin Hamiltonians, especially those with possibilities of frustration. Of particular “richness” is the behavior of spin liquids [1,2], and signatures of spin liquid behaviors have been observed in a variety of magnetic materials [3–5].

Quantum spin liquids are exotic phases of matter featuring topological order and long-range quantum entanglement, which motivated the proposal and exploration of techniques to engineer such systems for topological protection of quantum information [6,7]. To gain a more profound understanding of quantum spin liquids requires concerted experimental and computational efforts.

Digital quantum computers have been proposed as alternative and complementary approaches to the exploration of these strongly correlated quantum phases [8,9]. Systems with frustration caused by the lattice geometry or long-range interactions have been identified as promising avenues in the search for quantum spin liquids [10–16]. Spin liquid behavior in frustrated quantum systems has been explored with a variety of computational platforms, namely annealers [17], superconducting quantum circuits [18,19], and atom arrays [20].

Hamiltonian symmetries play a central role in the classification of Hamiltonian eigenfunctions, and in improving the efficiency and the accuracy of algorithms for the solution of the Schrödinger equation. The incorporation of symmetries in quantum simulation algorithms is an active research area with many important declinations, including qubit

reduction [21–25], the careful design of state preparation circuits [26], the introduction of symmetry violation penalties [27], and the adoption and refinement of post-selection and error-mitigation techniques. An important example, particularly for spin Hamiltonians, is spin symmetry: when a Hamiltonian operator  $\hat{H}$  commutes with the total spin and spin-z operators, respectively,  $\hat{S}^2$  and  $\hat{S}_z$ , there exists a basis of simultaneous eigenfunctions of  $\hat{H}$  and such constants of motion. Spin symmetry is encountered across a wide variety of situations relevant for the characterization of spin liquid behavior: from the Heisenberg model on a complete graph  $\hat{H} = \sum_{i<j} \mathbf{S}_i \cdot \mathbf{S}_j = (\hat{S}^2 - \sum_i \hat{S}_i^2)/2$ , to spin Hamiltonian providing a minimal model of magnetic correlations in molecular systems [28,29], and the electronic structure of molecules and materials [30–34].

In this work, we explore quantum circuits for the synthesis of spin eigenfunctions on quantum computers. Previous approaches typically concentrated on circuits for exact or controllably approximated encoding of general spin eigenstates [35] that require quantum resources (ancillae and multi-controlled multi-qubit gates) often beyond the capabilities of contemporary quantum hardware, or circuits for encoding of specific spin eigenstates [36,37], which have less generality but require less quantum resources.

Here, we investigate the balances among generality, accuracy, and computational costs in the encoding of spin eigenfunctions by quantum circuits, by pursuing two approaches: an exact recursive construction of spin eigenstates and a heuristic variational construction of approximate spin eigenstates.

The remainder of the present work is structured as follows. In Section 2, we present the two families of circuits studied in this work. In Section 3, we apply the proposed circuits to systems of three- and five-spin-1/2 particles on graphs with triangle connectivities, using classical simulators of quantum computers and quantum hardware. Conclusions are drawn in Section 4, and additional theoretical and implementation details are presented in the Appendixes A and B.

## 2. Methods

In this section, we describe our approaches to encode spin eigenstates on quantum computers. The exact recursive construction is presented in Section 2.1, focusing on the structure and computational cost of the corresponding quantum circuits. The heuristic variational construction is presented in Section 2.2, focusing on the Ansätze proposed and tested in the present work.

### 2.1. Exact Recursive Construction

In this section, we consider a system of  $n$  spin- $\frac{1}{2}$  particles, and our aim is to prepare such a system in an eigenfunction  $|\ell, m\rangle$  of the total spin operators  $\hat{S}^2$  and  $\hat{S}_z$  with eigenvalues  $\ell(\ell + 1)$  and  $m$ , respectively, with  $\ell = k/2$ ,  $k \in \{1, 2, \dots, n\}$  and  $m = -\ell, \dots, \ell$ . Following an established convention, we map the Hilbert space of a single spin-up particle onto that of a single qubit as

$$|\ell = 1/2, m = 1/2\rangle \rightarrow |0\rangle, \quad |\ell = 1/2, m = -1/2\rangle \rightarrow |1\rangle. \quad (1)$$

A single qubit can thus be prepared in a spin eigenfunction by applying to the initial state  $|0\rangle$  one of the following unitary transformations,

$$\hat{U}_{\ell=1/2, m=1/2} = \mathbb{1}, \quad \hat{U}_{\ell=1/2, m=-1/2} = X, \quad (2)$$

where  $X$  denotes the Pauli  $X$  operator, defined in Appendix B. A register of  $n = 2$  qubits can be prepared in a total spin eigenfunction using the quantum circuit shown in Figure 1, which uses a single CNOT gate, also defined in Appendix B.

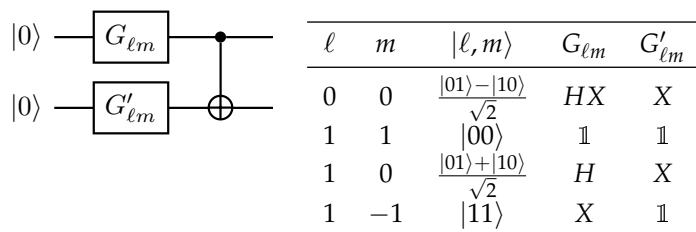


**Figure 1.** (Left): exact construction of total spin eigenfunctions for  $n = 2$  qubits. (Right): qubit representation of the total spin eigenfunction  $|\ell, m\rangle$  for  $n = 2$  qubits, and gates  $G_{\ell, m}$  used to encode it.

In the remainder of this section, we will present a recursive procedure to prepare  $n \geq 2$  qubits in a total spin eigenfunction. For  $n = 2$ , such a preparation was shown in Figure 1.

Let us now show that the possibility to prepare  $n \geq 2$  qubits into a total spin eigenfunction implies the possibility to prepare  $n + 1$  qubits into a total spin eigenfunction. The starting point is the angular momentum addition theorem,

$$|\ell_1, \ell_2, \ell, m\rangle = \sum_{m_1, m_2} C_{\ell_1, m_1, \ell_2, m_2}^{\ell, m} |\ell_1, m_1\rangle \otimes |\ell_2, m_2\rangle \tag{3}$$

where  $|\ell_1, m_1\rangle$ ,  $|\ell_2, m_2\rangle$ , and  $|\ell_1, \ell_2, \ell, m\rangle$  are eigenfunctions of the total spin operators with eigenvalues  $\ell_1, m_1, \ell_2, m_2$ , and  $\ell, m$ , respectively, and  $C_{\ell_1, m_1, \ell_2, m_2}^{\ell, m}$  is a Clebsch–Gordan coefficient. Here, our goal is to map  $|\ell_1, \ell_2, \ell, m\rangle$  onto a wave function of  $n + 1$  qubits. To this end, let us consider the case  $\ell_2 = 1/2$ , so that Equation (3) takes the form

$$|\ell_1, 1/2, \ell, m\rangle = \sum_{m_2} \psi_{m_2} |\ell_1, m - m_2\rangle \otimes |1/2, m_2\rangle, \quad \psi_{m_2} = C_{\ell_1, m - m_2, 1/2, m_2}^{\ell, m} \tag{4}$$

By the induction hypothesis,  $|\ell_1, m - m_2\rangle$  can be mapped onto an  $n$ -qubit wave function applying a quantum circuit  $\hat{U}_{\ell_1, m - m_2}$  to a register of  $n$  qubits prepared in  $|0\rangle^{\otimes n}$ . Writing

$$\psi_{1/2} = \cos(\theta/2), \quad \psi_{-1/2} = \sin(\theta/2) \tag{5}$$

for a suitable angle  $\theta \in [0, 2\pi)$  shows that the state  $|\ell_1, 1/2, \ell, m\rangle$  can be mapped onto an  $(n + 1)$ -qubit wave function, applying either of the the unitary transformations

$$\hat{U}_{\ell, m} = c_{n+1} \left( \hat{U}_{\ell_1, m+1/2} \hat{U}_{\ell_1, m-1/2}^\dagger \right) \hat{U}_{\ell_1, m-1/2} \otimes R_y(\theta) \tag{6}$$

$$= \bar{c}_{n+1} \hat{U}_{\ell_1, m-1/2} c_{n+1} \hat{U}_{\ell_1, m+1/2} R_{y, n+1}(\theta) \tag{7}$$

to a register of  $n + 1$  qubits prepared in  $|0\rangle^{\otimes(n+1)}$ . In Equations (6) and (7),  $R_{y, i}(\theta) = \exp(-i\theta Y_i/2)$  is a  $Y$  rotation of an angle  $\theta$  applied to qubit  $i$ , and the symbols  $c_i$  and  $\bar{c}_i$  indicate application of a unitary transformation when qubit  $i$  is in  $|0\rangle$  or  $|1\rangle$ , respectively. The unitary transformations in Equations (6) and (7) are equivalent to the quantum circuits shown in Figure 2.

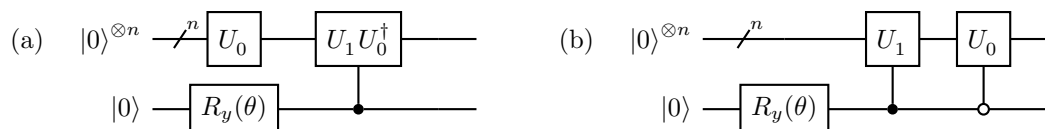


**Figure 2.** Quantum circuits for exact recursive construction of total spin eigenfunctions, with  $\hat{U}_0 = \hat{U}_{\ell_1, m-1/2}$  and  $\hat{U}_1 = \hat{U}_{\ell_1, m+1/2}$  to avoid clutter. The two circuits (a,b) are equivalent to each other, and Equations (6) and (7), respectively.

As a simple and relevant example, in Figure 3, we apply the exact recursive construction to  $n = 3$  spins. The gates  $G_0, G'_0, G_1, G'_1$  are defined as in the right portion of Figure 1, and implement the unitaries  $\hat{U}_{\ell_{01}, m-1/2}$  and  $\hat{U}_{\ell_{01}, m+1/2}$ , respectively, with

$$|\ell_{01} - 1/2| \leq \ell \leq \ell_{01} + 1/2. \tag{8}$$

Comparing Figures 2b and 3, this show that the latter circuit is simplified, in order to remove redundant gates.

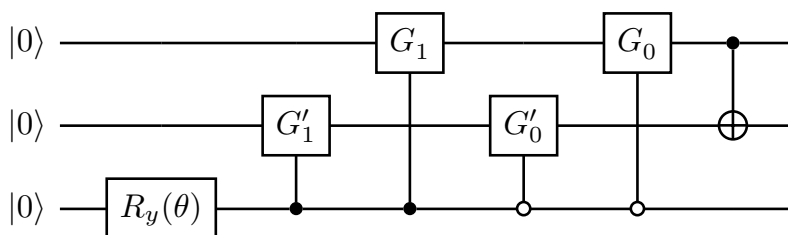


**Figure 3.** Illustration of the exact recursive construction for  $n = 3$  spins. The single-qubit gates  $G_k$  and  $G'_k$  are as listed in the right portion of Figure 1.

**Computational Cost**

Compared against previous approaches, the exact recursive construction presented here requires no ancillae [35], and applies to generic spin eigenfunctions [36]. However, it requires a number of single-qubit and CNOT gates scaling exponentially with  $n$ .

This circumstance can be understood considering the structure in Figure 2. Constructing an  $(n + 1)$ -qubit total spin eigenfunction requires two controlled  $n$ -qubit circuits and a single-qubit  $Y$  rotation. Denoting  $c_n, s_n$  the number of CNOT and single-qubit gates comprising the  $n$ -qubit circuit, respectively, one can easily see that the  $n(+1)$ -qubit circuit requires  $c_n$  Toffoli,  $s_n$  controlled single-qubit gates, and one additional single-qubit gate. By Lemmas 6.1 and 5.4 of [38], respectively, a Toffoli gate requires 8 CNOT and six single-qubit gates, and a controlled single-qubit gate requires two CNOT and two single-qubit gates. Therefore,  $c_{n+1} = 16c_n + 4s_n$  and  $s_{n+1} = 12c_n + 4s_n$ .

Numeric integration of these recursion relations, with the initial conditions  $c_2, s_2 = 1, 2$  as seen in Figure 2, gives  $c_n, s_n \simeq 3^n$ , which is exponential in the number of qubits. We remark that, in practice, circuit simplification techniques can lower this gate count, especially for total spin eigenfunctions with low entanglement.

**2.2. Heuristic Variational Construction**

The high computational cost of exact construction techniques for arbitrary spin eigenfunctions makes it desirable to propose less-expensive alternative strategies that are more suited to contemporary quantum devices. In this section, we present a technique for heuristic variational construction of approximate total spin eigenfunctions.

Simulations of many-body ground and excited states on contemporary quantum hardware frequently make use of parametrized families of wave functions, of the form  $|\Psi(\theta)\rangle = \hat{U}(\theta)|\Psi_0\rangle$ , where  $\hat{U}(\theta)$  is a quantum circuit comprising free parameters, and  $|\Psi_0\rangle$  is an initial wave function [39]. The best approximation to a target state within the set  $|\Psi(\theta)\rangle$  is chosen by minimizing a suitable cost function with respect to the parameters  $\theta$  in the quantum circuit. A prominent example is the variational quantum eigensolver [40], where the target state is the ground state of a Hamiltonian operator  $\hat{H}$ , and the cost function is the expectation value  $E(\theta) = \langle \Psi(\theta) | \hat{H} | \Psi(\theta) \rangle$  of the Hamiltonian over the state  $|\Psi(\theta)\rangle$ . A natural choice for the cost function is

$$C_{\ell, m}(\theta) = \left( \langle \hat{S}_z \rangle - m \right)^2 + \left( \langle \hat{S}^2 \rangle - \ell(\ell + 1) \right)^2 \tag{9}$$

where  $\langle \cdot \rangle$  denotes expectation value of an operator over the state  $\Psi(\theta)$ . In the present work, we also consider the possibility to fix the total spin of one or more qubit subsets

$\Omega_1, \dots, \Omega_r \subset \{0 \dots n - 1\}$  to a target value, respectively,  $\ell_1, \dots, \ell_r$ . To achieve this goal, we alter the cost function as follows,

$$C_{\ell_1, \dots, \ell_r, \ell, m}(\theta) = C_{\ell, m}(\theta) + \sum_{k=1}^r \left( \langle \hat{S}_{\Omega_k}^2 \rangle - \ell_k(\ell_k + 1) \right)^2, \tag{10}$$

where  $\hat{S}_{\Omega_k}^2$  denotes the total spin of subset  $\Omega_k$ . The functional  $C_{\ell_1, \dots, \ell_r, \ell, m}(\theta)$  takes value 0 provided that  $\Psi(\theta)$  is an eigenfunction of the operators  $\hat{S}_{\Omega_k}^2$ ,  $\hat{S}^2$ , and  $\hat{S}_z$  with eigenvalues  $\ell_k(\ell_k + 1)$ ,  $\ell(\ell + 1)$ , and  $m$ , respectively.

The gradient of the cost function Equation (10) is computed using the chain rule, and gradients of expectation values  $\langle \cdot \rangle$  are computed analytically, rather than by finite differences, using a suitable shift formula [41–45].

Ansätze

The quality of a variational simulation depends not only on the cost function, but also on the underlying ansatz, i.e., the map  $\theta \rightarrow |\Psi(\theta)\rangle$ . In the present work, we explore several Ansätze, with the goal of assessing and comparing their accuracy and efficiently in the approximation of total spin eigenfunctions.

First, we consider the following  $R_y$  ansatz [46],

$$|\Psi(\theta)\rangle = \prod_{k=1}^r \left[ \prod_{i=0}^{n-1} R_{y,i}(\theta_{k,i}) E \right] \prod_{i=0}^{n-1} R_{y,i}(\theta_{0,i}) |\Psi_0\rangle, \quad E = \prod_{(i,j) \in L} c_i X_j, \tag{11}$$

where  $|0\rangle^{\otimes n}$  is an initial wave function,  $m$  is the number of qubits,  $R_{y,i}(\theta) = \exp(-i\theta Y_i/2)$  is a  $Y$  rotation of an angle  $\theta$  applied to qubit  $i$ ,  $c_i X_j$  is a CNOT gate acting on qubits  $(i, j) \in L$ , and  $r$  is an integer denoting the number of times an entangling gate  $E$  followed by a layer of  $Y$  rotations is repeated. The  $R_y$  ansatz is illustrated in Figure 4 for  $r = 3$ .

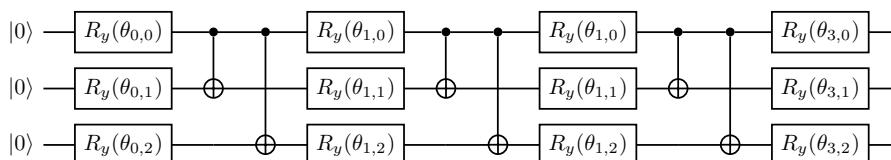


**Figure 4.** Illustration of the  $R_y$  ansatz, with CNOT gates acting on qubits (0,1) and (1,2), and initial state  $|\Psi_0\rangle = |0, 0, 0\rangle$ .

Next, we consider an ansatz inspired by time evolution. Reference [47] illustrated a recursive procedure for the preparation of an  $n$ -qubit system in a total spin eigenfunction. An  $(n - 1)$ -qubit system is prepared in a total spin eigenfunction  $|\ell, m\rangle_{n-1}$  and coupled with a qubit prepared in  $|1/2, 1/2\rangle$ . The system evolves under the action of a Heisenberg Hamiltonian with all-to-all coupling,  $\hat{H} = J \sum_{i < j=0}^{n-1} \mathbf{S}_i \cdot \mathbf{S}_j$ , leading to the wave-function

$$|\Psi(t)\rangle = e^{-it\hat{H}} |\ell, m\rangle_{n-1} \otimes |1/2, 1/2\rangle = \sum_{k=\pm 1} c_k(t) |\ell + k/2, m + 1/2\rangle. \tag{12}$$

Provided that the coefficients satisfy the relation

$$c_+(t) = \sqrt{\frac{\ell + m + 1}{2\ell + 1}}, \quad c_-(t) = \sqrt{\frac{\ell - m}{2\ell + 1}}, \tag{13}$$

the state  $|\Psi(t)\rangle$  is a total spin eigenfunction with eigenvalues  $\ell, m$ . Motivated by this result, following and adapting the construction of the QAOA method [48], we introduce

a variational form inspired by time evolution, shown in Figure 5. The Hamiltonian is represented as

$$\hat{H} = J \sum_{i<j=0}^{n-1} \mathbf{S}_i \cdot \mathbf{S}_j = J \sum_{i<j=0}^{n-2} \mathbf{S}_i \cdot \mathbf{S}_j + J \left[ \sum_{i=0}^{n-2} \mathbf{S}_i \right] \cdot \mathbf{S}_{n-1} = \hat{H}_0 + \hat{V}, \tag{14}$$

and in Figure 5a the time evolution operator is approximated with the following primitive Trotter formula [49–52],

$$e^{-it\hat{H}} \simeq e^{-it\hat{V}} e^{-it\hat{H}_0}. \tag{15}$$

In Figure 5b, we further impose the following primitive Trotter approximation,

$$e^{-itJ\sum_{ij} \mathbf{S}_i \cdot \mathbf{S}_j} \simeq \prod_{ij} e^{-itJ\mathbf{S}_i \cdot \mathbf{S}_j} = \prod_{ij} u_{ij}(tJ), \tag{16}$$

and substitute each unitary  $e^{-itJ\mathbf{S}_i \cdot \mathbf{S}_j}$  with a parametrized two-qubit gate of the kind shown in Figure 5c.

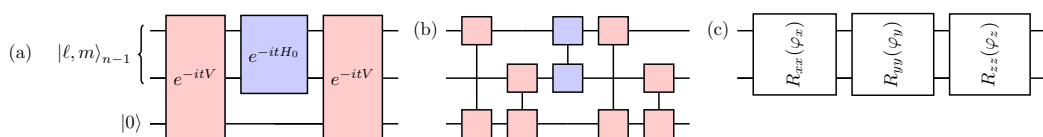


**Figure 5.** Time evolution-inspired variational form. (a) Time evolution under the Heisenberg Hamiltonian for  $r = 2$  steps and  $n = 3$  qubits is approximated with a primitive Trotter formula; in the first step of time evolution, the unitary  $e^{-it\hat{H}_0}$  is not applied in the first step of time evolution, since the top  $n - 1$  qubits are prepared in an eigenstate of  $\hat{H}_0$ . (b) Each unitary  $e^{-it\hat{H}_0}$  and  $e^{-it\hat{V}}$  (blue, red blocks in the left panel) is approximated by a product of unitary  $u_{ij}(tJ)$  (rectangles connected by a vertical line). (c) Each unitary  $u_{ij}(tJ)$  is replaced by a parametrized two-qubit gate.

### 3. Results

#### Computational Details.

We used IBM’s open-source Python library for quantum computing, Qiskit [53]. Qiskit provides tools for various tasks, such as creating quantum circuits, performing simulations, and computations on quantum devices. It also contains an implementation of the VQE algorithm, a hybrid quantum–classical algorithm that uses both quantum and classical resources to variationally optimize the cost function, and a classical exact eigensolver algorithm, against which to compare results. We then minimize the expectation value of the cost function with respect to the parameters of the variational circuit. The minimization is carried out through a classical optimization method [54–59]. In this work, we used the conjugate gradient [59] on the noiseless and deterministic statevector\_simulator of Qiskit. We then used the optimized parameters to compute expectation values on quantum hardware. We performed experiments on five-qubit devices available through IBM Quantum Experience, each with a quantum volume [60] of 32, namely, ibmq\_athens, ibmq\_santiago, and ibmq\_manila [61].

#### Error mitigation.

We employed readout-error mitigation (EM) [62–65] as implemented in Qiskit Ignis to correct measurement errors. We also used a noise extrapolation scheme, namely a simplified form of the Richardson extrapolation (RE), which uses additional CNOT gates at the minimum-energy VQE iterations to account for errors introduced by two-qubit entangling operations [66,67]. More specifically, each CNOT gate in the circuit is replaced with a product of  $2k + 1$  CNOT gates,  $cX \rightarrow cX^{2k+1}$ , and the expectation value  $A_k$  of an observable is extrapolated with a linear ansatz,

$$A_k = A_{\text{extrapolated}} + (2k + 1)\Delta. \tag{17}$$

Following reference [66], we call  $r = 2k + 1$  the “noise parameter”.

Tomography.

An important goal of the present work is to assess how faithfully a quantum circuit executed on a quantum device approximates a target wave function  $\psi_{\text{ideal}}$ . To answer this question, we compute the fidelity

$$F(\rho_{\text{circuit}}, \psi_{\text{ideal}}) = \langle \psi_{\text{ideal}} | \rho_{\text{circuit}} | \psi_{\text{ideal}} \rangle \tag{18}$$

between  $\psi_{\text{ideal}}$  and the density operator  $\rho_{\text{circuit}}$  prepared on the quantum hardware, and the purity of the former,

$$P(\rho_{\text{circuit}}) = \text{Tr}(\rho_{\text{circuit}}^2). \tag{19}$$

The density operator  $\rho_{\text{circuit}}$  is measured by quantum tomography [68], and Equations (18) and (19) are computed on the `statevector_simulator` of Qiskit based on the measurement outcomes.

Target problems.

In the present work, we consider systems of  $n = 3$  and  $n = 5$  spins on graphs with triangle connectivity, illustrated in Figure 6. For three-spin problems, our goal is to prepare total spin eigenfunctions starting from total spin eigenfunctions of the left spins (labeled 0,1 in Figure 6a). For five-spin problems, we start from total spin eigenfunctions of the left spins (labeled 0,1 in Figure 6b and henceforth L), of the left and central spins (labeled 0,1,2 in Figure 6b and henceforth LC), and of the right spins (labeled 3,4 in Figure 6b and henceforth R).

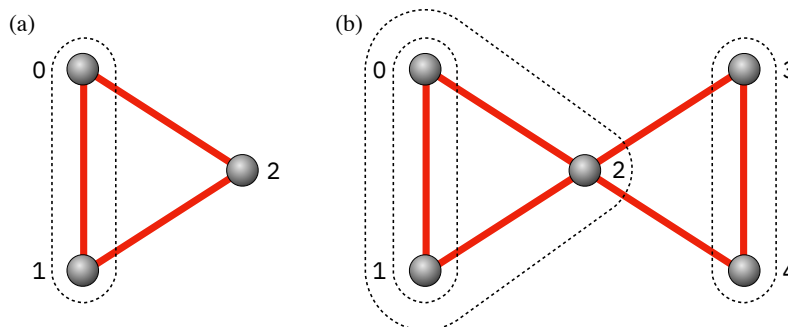


**Figure 6.** Representation of a set of three (a) and five (b) spins on graphs with triangle connectivity. Black circles represent spins, labeled from 0 to 4, and red lines connect neighboring qubits. Black dashes lines represent subsets  $\Omega_{01}$  (in panel (a)) and  $\Omega_L = \Omega_{01}$ ,  $\Omega_{LC} = \Omega_{012}$ ,  $\Omega_R = \Omega_{34}$  (in panel (b)).

### 3.1. Exact Recursive Construction

In Figure 7, we demonstrate the exact recursive construction for systems of  $n = 3$  spins prepared in the representative states  $|\ell_{01} = 0, \ell = 1/2, m = -1/2\rangle$  and  $|\ell_{01} = 1, \ell = 3/2, m = -1/2\rangle$ . We focus on the evaluation of the total spin operators  $\hat{S}_{01}^2$  (total spin of qubits 0 and 1),  $\hat{S}^2$ , and  $\hat{S}_z$ . As naturally expected, the use of EM and EM + RE significantly improves the agreement between exact and simulated values for these quantities.

Two natural questions are whether the improved quality observed for the expectation values of spin operators translates to generic observables, and what decoherence mechanisms are responsible for the deviations seen in raw hardware simulations.

To address these questions, in Table 1 we compute the fidelity and purity of the state  $\rho_{\text{circuit}}$ , respectively, Equations (18) and (19). We observe  $F(\rho_{\text{circuit}}, \psi_{\text{ideal}}) < 1$ , which mirrors the deviations between exact and simulated expectation values of spin operators. Furthermore,  $P(\rho_{\text{circuit}}) < 1$  in raw hardware simulations, indicates that qubits are depolarized by decoherence. The combined use of EM + RE increases the fidelity towards one, indicating a more faithful representation of the quantities measured on the device.

Fidelities are extrapolated as shown in the right panel of Figure 8, where analogous results are presented for all the total spin eigenfunctions of  $n = 3$  qubits.

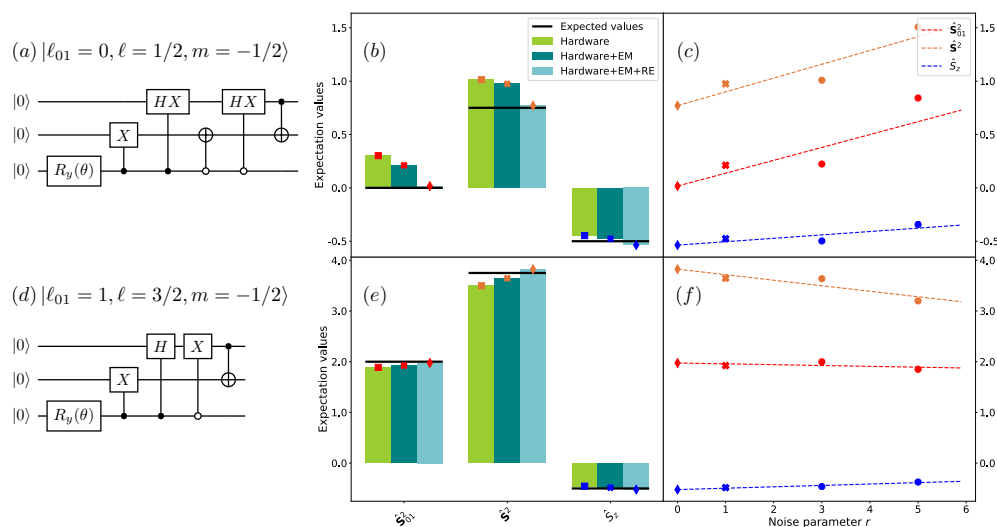


**Figure 7.** Results from the exact recursive construction, for systems of  $n = 3$  spins prepared in  $|\ell_{01} = 0, \ell = 1/2, m = -1/2\rangle$  and  $|\ell_{01} = 1, \ell = 3/2, m = -1/2\rangle$  ((a–f), respectively), on the `ibmq_athens` device. (a,d): Quantum circuits to encode the target states. (b,e): Expectation values of the total spin operators  $\hat{S}_{01}^2$ ,  $\hat{S}^2$ , and  $\hat{S}_z$  from raw hardware simulations (light green, leftmost bar), simulations employing readout error mitigation (EM, teal, center bar), and simulations employing readout error mitigation and Richardson extrapolation (EM + RE, light blue, rightmost bar). Exact values are marked by black lines. (c,f): Extrapolation of the expectation values in the middle panels versus number of CNOT gates. Crosses ( $r = 1$ ), circles ( $r = 3.5$ ), and diamonds ( $r = 0$ ) denote error-mitigated, noise-amplified, and extrapolated quantities, respectively. Red, yellow, and blue symbols indicate  $\hat{S}_{01}^2$ ,  $\hat{S}^2$ , and  $\hat{S}_z$ , respectively.

**Table 1.** Fidelity and purity of the state  $\rho_{\text{circuit}}$  for systems of  $n = 3$  spins prepared in the states  $|\ell_{01} = 0, \ell = 1/2, m = -1/2\rangle$  and  $|\ell_{01} = 1, \ell = 3/2, m = -1/2\rangle$  (top, bottom, respectively) using exact recursive construction. The fidelity is extrapolated as shown in the right panel of Figure 8.

$(\ell_{01}, \ell, m)$	$F(\rho_{\text{circuit}}, \psi_{\text{ideal}})$ (Raw)	$P(\rho_{\text{circuit}})$ (Raw)	$F(\rho_{\text{circuit}}, \psi_{\text{ideal}})$ (EM + RE)
$(0, 1/2, -1/2)$	0.78708	0.79982	$0.9720 \pm 0.0306$
$(1, 3/2, -1/2)$	0.86417	0.90659	$0.9944 \pm 0.0057$

In Figure 9, we apply the exact recursive construction to systems of  $n = 5$  spins, using the `qasm_simulator` with noise model from `ibmq_athens`, and `ibmq_athens`. We focus on the states  $|\ell_L = 0, \ell_{LC} = 1/2, \ell_R = 0, \ell = 1/2, m = -1/2\rangle$  and  $|\ell_L = 0, \ell_{LC} = 1/2, \ell_R = 1, \ell = 1/2, m = -1/2\rangle$ . Although the trends seen for  $n = 3$  qubits, especially the beneficial impact of EM + RE techniques, are confirmed, a significant difference exists between Figures 7 and 9: in the latter case, error mitigation techniques do not close the gap between exact and simulated expectation values. The same phenomenon is observed in Figure 10, where we compute the fidelities between exact and simulated total spin eigenfunctions, for several representative states, using `qasm_simulator` and `ibmq_manila`. The different efficacy of error mitigation techniques for  $n = 3$  and  $n = 5$  qubits is an important observation of the present work, and it will be discussed in detail in the conclusions.

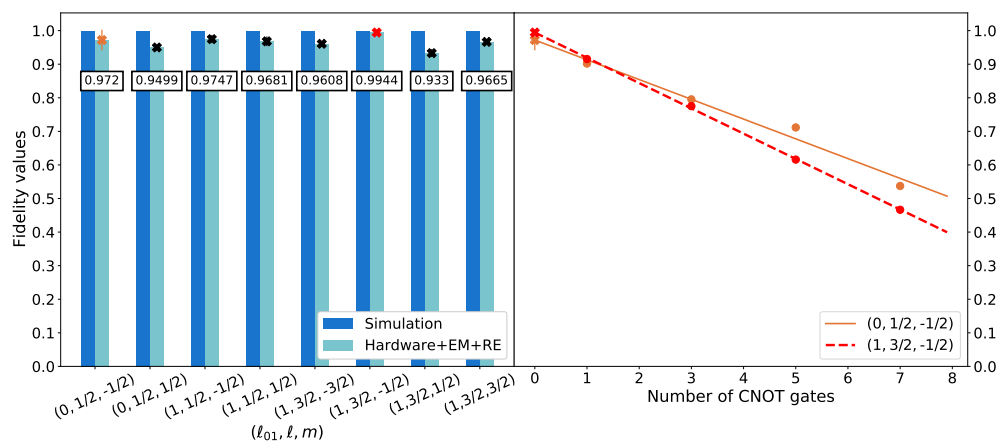


**Figure 8.** Left: fidelities of  $n = 3$  qubits prepared in the total spin eigenstates  $|\ell_{01}, \ell, m\rangle$ . Fidelities are computed through qubit state tomography employing readout error mitigation (EM), and gate noise is mitigated by a Richardson extrapolation (RE). Right: Richardson extrapolation of the error-mitigated fidelities for systems of  $n = 3$  qubits prepared in the states  $|\ell_{01} = 0, \ell = 1/2, m = -1/2\rangle$  (yellow symbols) and  $|\ell_{01} = 1, \ell = 3/2, m = -1/2\rangle$  (red symbols) with the exact recursive procedure. Circles and crosses denote measured an extrapolated quantities, respectively.

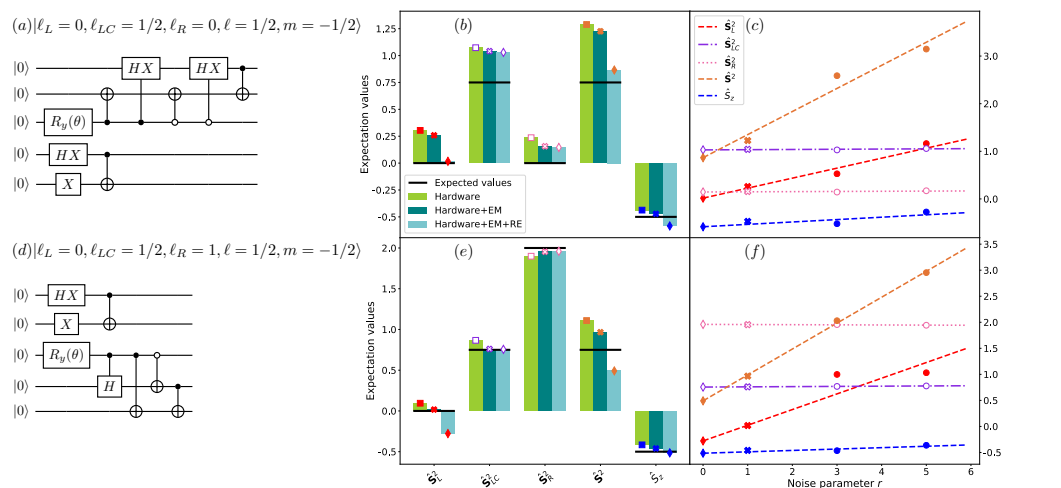


**Figure 9.** Results from the exact recursive construction, for systems of  $n = 5$  spins prepared in the wave functions  $|s_L = 0, s_{LC} = 1/2, s_R = 0, s = 1/2, s_z = -1/2\rangle$  and  $|s_L = 0, s_{LC} = 1/2, s_R = 1, s = 1/2, s_z = -1/2\rangle$  ((a–f), respectively) on the `ibmq_athens` device. (a,d): Quantum circuits to encode the target states. (b,e): Expectation values of the total spin operators  $\hat{S}_{01}^2, \hat{S}^2$ , and  $\hat{S}_z$  from raw hardware simulations (light green, leftmost bar), simulations employing readout error mitigation (EM, teal, center bar), and simulations employing readout error mitigation and Richardson extrapolation (EM + RE, light blue, rightmost bar). Exact values are marked by black lines. (c,f): Extrapolation of the expectation values in the middle panels versus number of CNOT gates. Crosses ( $r = 1$ ), circles ( $r = 3.5$ ), and diamonds ( $r = 0$ ) denote error-mitigated, noise-amplified, and extrapolated quantities, respectively. Red, yellow, and blue symbols indicate  $\hat{S}_{01}^2, \hat{S}^2$ , and  $\hat{S}_z$ , respectively.

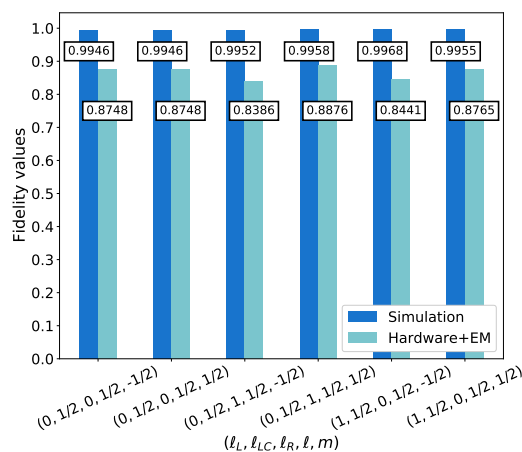


**Figure 10.** Fidelities between exact and simulated total spin eigenfunctions for  $n = 5$  qubits, computed using `qasm_simulator` and `ibmq_manila`.

### 3.2. Heuristic Variational Construction

In this section, we assess the accuracy and performance of VQE-based quantum circuits for approximate encoding of total spin eigenstates. Unlike in the case of exact recursive construction, variationally optimized circuits are not guaranteed to accurately approximate all the total spin eigenstates. For each ansatz explored in the present work, we thus begin our analysis by assessing the ansatz accuracy using classical simulators of noiseless quantum hardware, and we finally demonstrate the corresponding quantum circuits on IBM devices.

#### 3.2.1. $R_y$ Ansatz

In Figure 11, we show the optimized cost function  $C_{\text{opt}}(\ell_{01}, \ell, m) = \min_{\theta} C_{\ell, m, \ell_{01}}(\theta)$  for the  $R_y$  ansatz with  $n = 3$  qubits and the connectivity in Figure 4, as a function of the ansatz depth  $r$ , as defined in Equation (11). As seen, the choice  $r \geq 2$  ensures minimization of the cost function within single numeric precision across all spin eigenstates. In Table 2, we list the fidelity between the state  $\Psi_{\text{opt}} = \Psi(\theta_{\text{opt}})$  and the target eigenstate  $|\ell_{01}, \ell, m\rangle$ . As seen, the fidelity is equal to 1 except for the Dicke states  $|1, 3/2, \pm 1/2\rangle$  [69–73]. This is not unexpected, as the Dicke states are the most entangled  $n$ -spin states and, therefore, the most difficult targets for a variational optimization.

In Figure 12, we compute the spin operators  $\hat{S}^2, \hat{S}_z$  and  $\hat{S}_{01}^2$  using `qasm_simulator` with noise model from `ibmq_athens` and on the device `ibmq_athens`, and the  $R_y$  ansatz with depth  $r = 3$ . Similar trends are seen in both cases, with the combined use of EM + RE systematically improving results. It is clear that the noise models do not faithfully emulate the noise observe in our experiments, as readily seen when comparing the data in Figure 12. Given that the results are highly sensitive to noise affecting the qubits, it will be important to investigate these noise sources further and determine the extent to which they can be mitigated.

**Table 2.** Fidelities of optimal quantum circuits for  $n = 3$  qubits using the  $R_y$  ansatz with depth  $r = 3$ , computed with `statevector_simulator`.

$(\ell_{01}, \ell, m)$	$ \langle \psi_{\text{ideal}}   \Psi_{\text{opt}} \rangle ^2$
$(0, 1/2, -1/2)$	1.000000
$(0, 1/2, 1/2)$	1.000000
$(1, 1/2, -1/2)$	1.000000
$(1, 1/2, 1/2)$	1.000000
$(1, 3/2, -3/2)$	1.000000
$(1, 3/2, -1/2)$	0.396621
$(1, 3/2, 1/2)$	0.024675
$(1, 3/2, 3/2)$	1.000000

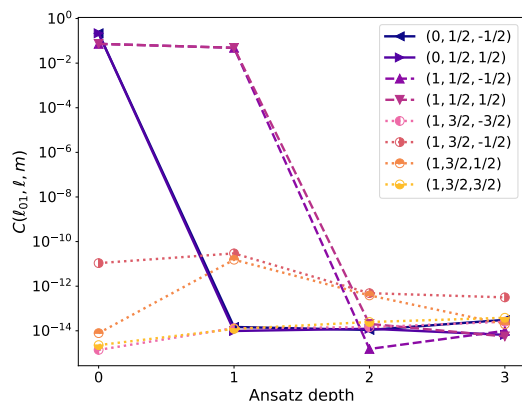


**Figure 11.** Cost function values  $C_{\text{opt}}$  of optimal quantum circuits for  $n = 3$  qubits using the  $R_y$  ansatz with depth  $r = 3$ , computed with `statevector_simulator`. The ideal value of the cost function is zero.

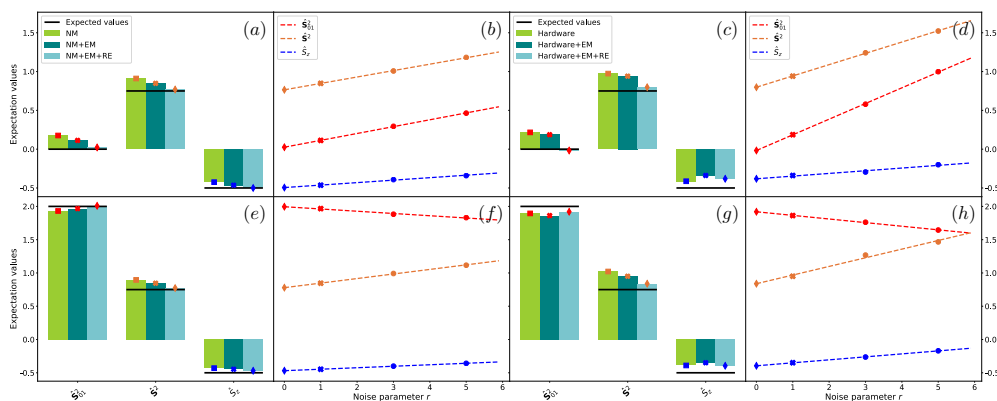


**Figure 12.** Bar charts: expectation values of the spin operators  $\hat{S}^2$ ,  $\hat{S}_x$ , and  $\hat{S}_{01}^2$  for systems of  $n = 3$  qubits prepared in  $|0, 1/2, -1/2\rangle$  (12 a,c) and  $|1, 1/2, -1/2\rangle$  (e,g) using `qasm_simulator` with noise model from `ibmq_athens` (a,e) and on the device `ibmq_athens` (c,g) and the  $R_y$  ansatz with depth  $r = 3$ . (b,d,f,h): Richardson extrapolation analysis for the expectation values shown in the bar charts. The vertical scales are matched to the scales in the accompanying bar chart.

While the combination of EM and RE reduces the deviations between exact and simulated quantities, it does not completely remove them. To document this observation, in Figure 13, we compute the fidelity between optimal exact total spin eigenstates and VQE wave functions computed with `statevector_simulator` (seen in Table 2) and on `ibmq_athens`. As seen, decoherence significantly affects the fidelities of the obtained wave functions.

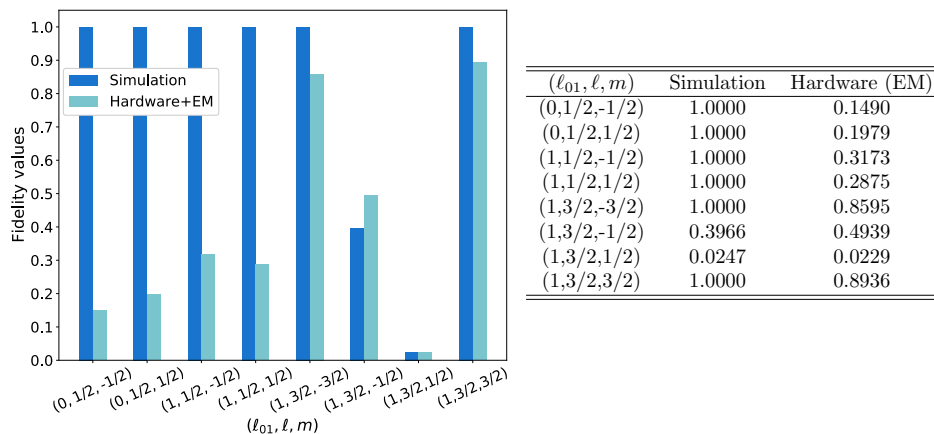


**Figure 13.** Fidelities for  $n = 3$  between exact total spin eigenstates and VQE wave functions computed with `statevector_simulator` and `ibmq_athens` (light, dark blue columns).

### 3.2.2. Time-Evolution Variational Form

We now consider the time-evolution variational form. Unlike in the case of  $R_y$ , where the initial state is customarily fixed to  $|0\rangle^{\otimes n}$ , here, the initial state is set to

$$\begin{aligned} |\psi(0)\rangle &= |110\rangle && \text{for } |1, 3/2, -1/2\rangle \\ |\psi(0)\rangle &= \frac{|01\rangle+|10\rangle}{\sqrt{2}}|0\rangle && \text{for } |1, 3/2, 1/2\rangle \end{aligned} \tag{20}$$

For  $r \geq 2$  repetitions, the time-evolution variational form returned  $C_{\text{opt}} < 10^{-18}$  and fidelity  $F > 0.9999$  for all total spin eigenfunctions, including Dicke states. On the other hand, it should be noted that the better accuracy of the time-evolution variational form corresponds to a higher computational cost, quantified in Table 3.

In Figure 14, we show the expectation values of the total spin operators for  $n = 3$  qubits, using the time-evolution variational form, computed with `statevector_simulator` (seen in Table 2) and on `ibmq_santiago`. The higher computational cost of the time-evolution variational form, compared with the  $R_y$  variational form, results in an increased sensitivity to noise, and ultimately in a worse agreement between exact and simulated quantities, a trend especially pronounced on the actual quantum device.

**Table 3.** Circuit depth required to approximate three-qubit total spin eigenstates using the time-evolution variational form with  $r = 2$  repetitions from `statevector_simulator` (full connectivity, single-qubit, and CNOT native gates) and `ibmq_santiago` (linear connectivity, device-specific native gates).

$(\ell_{01}, \ell, m)$	$d_{\text{statevector\_simulator}}$	$d_{\text{ibmq\_santiago}}$
$(0, 1/2, -1/2)$	76	117
$(0, 1/2, 1/2)$	76	118
$(1, 1/2, -1/2)$	76	120
$(1, 1/2, 1/2)$	76	118
$(1, 3/2, -3/2)$	76	117
$(1, 3/2, -1/2)$	76	119
$(1, 3/2, 1/2)$	76	126
$(1, 3/2, 3/2)$	65	94

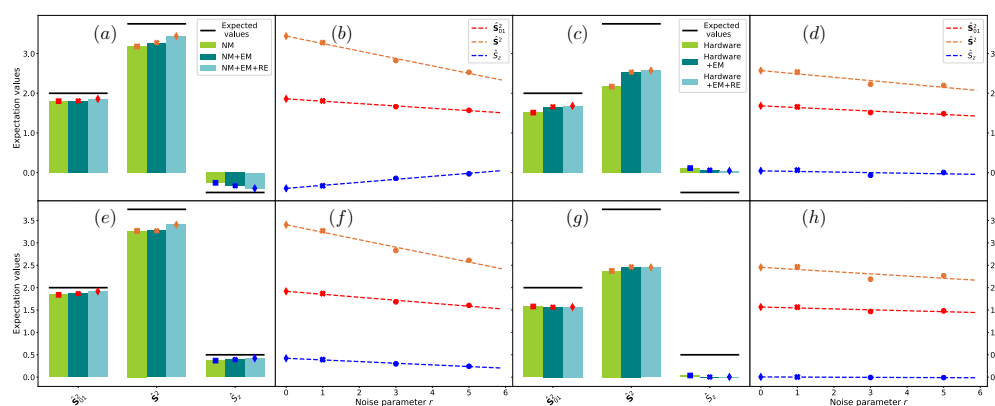


**Figure 14.** Bar charts: expectation values of the spin operators  $\hat{S}^2$ ,  $\hat{S}_z$ , and  $\hat{S}_{01}^2$  for systems of  $n = 3$  qubits prepared in  $|0, 1/2, -1/2\rangle$  (a,c) and  $|1, 1/2, -1/2\rangle$  (e,g) using the `ibmq_santiago` with noise model from `ibmq_santiago` (a,e) and on the device `ibmq_santiago` (c,g) and the time-evolution variational form. (b,d,f,h): Richardson extrapolation analysis for the expectation values shown in the bar charts. The vertical scales are matched to the scales in the accompanying bar chart.

## 4. Conclusions

In this work, quantum circuits for the exact and approximate preparation of total spin eigenfunctions on quantum computers were presented. We described two families

of circuits, representative of two different approaches to address this problem. First, we presented a recursive construction of total spin eigenfunctions based on the addition theorem of angular momentum, which we demonstrated for systems of three- and five-spin systems on graphs with triangle connectivity on IBM quantum devices. The approach is simple to understand and implement, and it guarantees exact mapping of total spin eigenfunctions on multi-qubit wave functions, without making use of ancillary qubits. On the other hand, its computational cost is at worst exponential in the number of qubits, which limits applications to large systems.

In addition, we presented a heuristic approximation of total spin eigenfunctions based on the variational optimization of a suitable cost function. The approach does not guarantee exact mapping of total spin eigenfunctions on multi-qubit wave functions. On the other hand, the heuristic variational approximation lends itself to simulations on contemporary quantum hardware, as it relies on families of quantum circuits whose computational costs can, by construction, fit within the computational budget allowed by a certain device.

We showed the effect of errors on the simulation of total spin eigenfunctions by performing experiments on actual quantum devices. We observed that qubit decoherence and gate errors cause significant infidelities between target and simulated wave functions. The extent of such a phenomenon depends on the number of spins as well as on the simulated circuit. We note particular problems with variational simulations of the most strongly correlated states, such as the Dicke states for  $n = 3$  spins, as well as topologies, such as  $n = 5$  spins in a bow-tie, with the four-way coordinated center spin.

Using the exact recursive construction, for  $n = 3$  qubits and  $n = 5$  qubits (as documented in Figures 8 and 10), infidelities are  $\sim 0.05$  and  $\sim 0.15$ , respectively, and roughly consistent across various spin eigenfunctions.

Larger and less-uniform infidelities are seen for  $n = 3$  qubits when VQE is used (Figure 13). These infidelities translate into significant deviations between the exact and simulated observables, as seen in Figure 14.

We demonstrate the effect of state-of-the-art error mitigation techniques to reduce the impact of measurement and gate errors on such results. To start with, systems with 3 qubits will have less error than 5, due to the different size and topology of these systems.

Of particular significance is the performance of the Richardson extrapolation, which breaks down for some of the  $n = 5$  qubits using the exact recursive construction (see Figure 9) and some of the  $n = 3$  qubits with very deep variational circuits (see Figure 14). In the case of  $n = 5$  qubits, we ascribe this effect mainly to the problem of frequency crosstalk for the central qubit of the bow tie topology, which needs to couple to four other closely valued (but different) frequency qubits. This problem will have to be solved if we are ever going to look at strongly coupled spin qubits in spin liquids. Ideally, the next system to study would be bow-tie (Figure 6) with the four corners (pairs (0,3) and (1,4)) also connected, with minimal connectivity.

**Author Contributions:** Conceptualization, D.E.G. and B.J.; methodology, A.C. and B.J.; software, A.C.; validation, A.C., D.E.G., B.J. and M.M.; formal analysis, A.C., D.E.G., B.J. and M.M.; investigation, A.C., D.E.G., B.J. and M.M.; resources, D.E.G.; data curation, A.C. and M.M.; writing—original draft preparation, A.C.; writing—review and editing, A.C., D.E.G., B.J. and M.M.; visualization, A.C. and M.M.; supervision, D.E.G. and B.J. All authors have read and agreed to the published version of the manuscript.

**Funding:** Partial funding was provided by the US Department of Energy, Office of Science, National Quantum Information Science Research Centers, Quantum Science Center.

**Institutional Review Board Statement:** Not applicable.

**Informed Consent Statement:** Not applicable.

**Data Availability Statement:** The data presented in this study are available upon reasonable request from the corresponding author.

**Acknowledgments:** A.C. and D.E.G. acknowledge the Università degli Studi di Milano INDACO Platform for providing resources that contributed to the results reported in this work.

**Conflicts of Interest:** The authors declare no conflict of interest.

**Appendix A. Structure of Total Spin Eigenfunctions**

In this section, we list the total spin eigenfunctions explored in the present study, for  $n = 3$  and  $n = 5$  spins, respectively, in Tables A1 and A2.

**Table A1.** Total spin eigenfunctions for systems of  $n = 3$  spins.

$\ell_{01}$	$\ell$	$m$	$ \ell_{01}, \ell, m\rangle$
0	1/2	-1/2	$\frac{1}{\sqrt{2}}( 011\rangle -  101\rangle)$
0	1/2	1/2	$\frac{1}{\sqrt{2}}( 100\rangle -  010\rangle)$
1	1/2	-1/2	$\frac{1}{\sqrt{6}}( 011\rangle +  101\rangle) - \frac{2}{\sqrt{3}} 110\rangle$
1	1/2	1/2	$\frac{1}{\sqrt{6}}( 100\rangle +  010\rangle) - \frac{2}{\sqrt{3}} 001\rangle$
1	3/2	-3/2	$ 111\rangle$
1	3/2	-1/2	$\frac{1}{\sqrt{3}}( 011\rangle +  101\rangle +  110\rangle)$
1	3/2	1/2	$\frac{1}{\sqrt{3}}( 100\rangle +  010\rangle +  001\rangle)$
1	3/2	3/2	$ 000\rangle$

**Table A2.** Six total spin eigenfunctions for systems of  $n = 5$  spins with  $\ell_{LC} = 1/2$  and  $(\ell_L, \ell_R) \in \{(0,0), (0,1), (1,0)\}$ .

$\ell_L$	$\ell_{LC}$	$\ell_R$	$\ell$	$m$	$ \ell_L, \ell_{LC}, \ell_R, \ell, m\rangle$
0	1/2	0	1/2	-1/2	$\frac{1}{2}( 01\rangle -  10\rangle) 1\rangle( 01\rangle -  10\rangle)$
0	1/2	0	1/2	1/2	$\frac{1}{2}( 01\rangle -  10\rangle) 0\rangle( 01\rangle -  10\rangle)$
0	1/2	1	1/2	-1/2	$\sqrt{\frac{1}{3}}( 01\rangle -  10\rangle)\left[\frac{1}{2} 1\rangle( 01\rangle +  10\rangle) -  011\rangle\right]$
0	1/2	1	1/2	1/2	$\sqrt{\frac{1}{3}}( 01\rangle -  10\rangle)\left[ 100\rangle - \frac{1}{2} 0\rangle( 01\rangle +  10\rangle)\right]$
1	1/2	0	1/2	-1/2	$\sqrt{\frac{1}{3}}\left[\frac{1}{2}( 01\rangle +  10\rangle) 1\rangle -  110\rangle\right]( 01\rangle -  10\rangle)$
1	1/2	0	1/2	1/2	$\sqrt{\frac{1}{3}}\left[ 001\rangle - \frac{1}{2}( 01\rangle +  10\rangle) 0\rangle\right]( 01\rangle -  10\rangle)$

**Appendix B. Quantum Computing Terms and Symbols**

In Figure A1, we illustrate the quantum operations used in the present work. Single-qubit rotations are exponentials of single-qubit Pauli operators, for example,  $R_x(\theta) = \exp(-i\theta X/2)$ . Single-qubit Pauli operators are equal to special single-qubit Pauli rotations up to a global phase, for example,  $X = R_x(\pi/2)$ . Single-qubit operations in the Clifford group (Hadamard,  $S$  and  $T$  gates) are equal to special single-qubit Pauli rotations up to a global phase, namely  $S = R_z(\pi/2)$ ,  $T = R_z(\pi/4)$ , and  $H = \exp(-i\pi/2(X + Z))$ .

The CNOT gate is sometimes denoted  $\text{CNOT}_{ij}$ , where  $i$  and  $j$  are called the control and target qubit, respectively, and applies an  $X$  transformation to its target qubit ( $\oplus$  symbol) if its control qubit ( $\bullet$  symbol) is in the state  $|1\rangle$ , the cU can be written as a product of up to two CNOT gates and four single-qubit gates, and the SWAP gate can be written as a product of three CNOT gates,  $\text{SWAP}_{ij} = \text{CNOT}_{ij}\text{CNOT}_{ji}\text{CNOT}_{ij}$ .

name	symbol	matrix	name	symbol	matrix	name	symbol	matrix
X rotation		$\begin{bmatrix} \cos(\theta) & -i\sin(\theta) \\ -i\sin(\theta) & \cos(\theta) \end{bmatrix}$	Y rotation		$\begin{bmatrix} \cos(\theta) & -\sin(\theta) \\ \sin(\theta) & \cos(\theta) \end{bmatrix}$	Z rotation		$\begin{bmatrix} e^{-i\theta} & 0 \\ 0 & e^{i\theta} \end{bmatrix}$
Pauli X		$\begin{bmatrix} 0 & 1 \\ 1 & 0 \end{bmatrix}$	Pauli Y		$\begin{bmatrix} 0 & -i \\ i & 0 \end{bmatrix}$	Pauli Z		$\begin{bmatrix} 1 & 0 \\ 0 & -1 \end{bmatrix}$
Hadamard		$\frac{1}{\sqrt{2}} \begin{bmatrix} 1 & 1 \\ 1 & -1 \end{bmatrix}$	S gate		$\begin{bmatrix} 1 & 0 \\ 0 & i \end{bmatrix}$	T gate		$\begin{bmatrix} 1 & 0 \\ 0 & e^{i\pi/4} \end{bmatrix}$
Z measurement		$p(z) =  \langle z \Psi\rangle ^2$	general measurement		$p(k) =  \langle \varphi_k \Psi\rangle ^2$	post-selection		$k = k_0$
CNOT		$\begin{bmatrix} 1 & 0 & 0 & 0 \\ 0 & 0 & 0 & 1 \\ 0 & 0 & 1 & 0 \\ 0 & 1 & 0 & 0 \end{bmatrix}$	controlled-U		$\begin{bmatrix} 1 & 0 & 0 & 0 \\ 0 & u_{00} & 0 & u_{10} \\ 0 & 0 & 1 & 0 \\ 0 & u_{10} & 0 & u_{11} \end{bmatrix}$	SWAP		$\begin{bmatrix} 1 & 0 & 0 & 0 \\ 0 & 0 & 1 & 0 \\ 0 & 1 & 0 & 0 \\ 0 & 0 & 0 & 1 \end{bmatrix}$

**Figure A1.** Examples of quantum gates and circuit elements. From top to bottom: single-qubit rotations, single-qubit Pauli operators, single-qubit operations in the Clifford group, measurements, and two-qubit gates. Adapted from reference [34].

## References

- Wen, X.G. Colloquium: Zoo of quantum-topological phases of matter. *Rev. Mod. Phys.* **2017**, *89*, 041004. [\[CrossRef\]](#)
- Sachdev, S. Topological order, emergent gauge fields, and Fermi surface reconstruction. *Rep. Prog. Phys.* **2018**, *82*, 014001. [\[CrossRef\]](#) [\[PubMed\]](#)
- Fu, M.; Imai, T.; Han, T.H.; Lee, Y.S. Evidence for a gapped spin-liquid ground state in a Kagome Heisenberg antiferromagnet. *Science* **2015**, *350*, 655–658. [\[CrossRef\]](#) [\[PubMed\]](#)
- Banerjee, A.; Lampen-Kelley, P.; Knolle, J.; Balz, C.; Aczel, A.A.; Winn, B.; Liu, Y.; Pajerowski, D.; Yan, J.; Bridges, C.A.; et al. Excitations in the field-induced quantum spin liquid state of  $\alpha$ -RuCl<sub>3</sub>. *npj Quantum Mater.* **2018**, *3*, 1–7. [\[CrossRef\]](#)
- Anderson, P.W. The resonating valence bond state in La<sub>2</sub>CuO<sub>4</sub> and superconductivity. *Science* **1987**, *235*, 1196–1198. [\[CrossRef\]](#) [\[PubMed\]](#)
- Kitaev, A.Y. Fault-tolerant quantum computation by anyons. *Ann. Phys.* **2003**, *303*, 2–30. [\[CrossRef\]](#)
- Nayak, C.; Simon, S.H.; Stern, A.; Freedman, M.; Sarma, S.D. Non-Abelian anyons and topological quantum computation. *Rev. Mod. Phys.* **2008**, *80*, 1083. [\[CrossRef\]](#)
- Georgescu, I.M.; Ashhab, S.; Nori, F. Quantum simulation. *Rev. Mod. Phys.* **2014**, *86*, 153. [\[CrossRef\]](#)
- Bauer, B.; Bravyi, S.; Motta, M.; Kin-Lic Chan, G. Quantum algorithms for quantum chemistry and quantum materials science. *Chem. Rev.* **2020**, *120*, 12685–12717. [\[CrossRef\]](#)
- Savary, L.; Balents, L. Quantum spin liquids: A review. *Rep. Prog. Phys.* **2016**, *80*, 016502. [\[CrossRef\]](#)
- Rokhsar, D.S.; Kivelson, S.A. Superconductivity and the quantum hard-core dimer gas. *Phys. Rev. Lett.* **1988**, *61*, 2376. [\[CrossRef\]](#) [\[PubMed\]](#)
- Sachdev, S. Kagomé-and triangular-lattice Heisenberg antiferromagnets: Ordering from quantum fluctuations and quantum-disordered ground states with unconfined bosonic spinons. *Phys. Rev. B* **1992**, *45*, 12377. [\[CrossRef\]](#) [\[PubMed\]](#)
- Misguich, G.; Serban, D.; Pasquier, V. Quantum dimer model on the kagome lattice: Solvable dimer-liquid and Ising gauge theory. *Phys. Rev. Lett.* **2002**, *89*, 137202. [\[CrossRef\]](#)
- Moessner, R.; Sondhi, S.L. Resonating valence bond phase in the triangular lattice quantum dimer model. *Phys. Rev. Lett.* **2001**, *86*, 1881. [\[CrossRef\]](#)
- Read, N.; Sachdev, S. Large- $N$  expansion for frustrated quantum antiferromagnets. *Phys. Rev. Lett.* **1991**, *66*, 1773. [\[CrossRef\]](#) [\[PubMed\]](#)
- Samajdar, R.; Ho, W.W.; Pichler, H.; Lukin, M.D.; Sachdev, S. Quantum phases of Rydberg atoms on a Kagome lattice. *Proc. Natl. Acad. Sci. USA* **2021**, *118*, e2015785118. [\[CrossRef\]](#)
- Zhou, S.; Green, D.; Dahl, E.D.; Chamon, C. Experimental realization of classical  $\mathbb{Z}_2$  spin liquids in a programmable quantum device. *Phys. Rev. B* **2021**, *104*, L081107. [\[CrossRef\]](#)
- Song, C.; Xu, D.; Zhang, P.; Wang, J.; Guo, Q.; Liu, W.; Xu, K.; Deng, H.; Huang, K.; Zheng, D.; et al. Demonstration of topological robustness of anyonic braiding statistics with a superconducting quantum circuit. *Phys. Rev. Lett.* **2018**, *121*, 030502. [\[CrossRef\]](#)
- Andersen, C.K.; Remm, A.; Lazar, S.; Krinner, S.; Lacroix, N.; Norris, G.J.; Gabureac, M.; Eichler, C.; Wallraff, A. Repeated quantum error detection in a surface code. *Nat. Phys.* **2020**, *16*, 875–880. [\[CrossRef\]](#)
- Semeghini, G.; Levine, H.; Keesling, A.; Ebadi, S.; Wang, T.T.; Bluvstein, D.; Verresen, R.; Pichler, H.; Kalinowski, M.; Samajdar, R.; et al. Probing topological spin liquids on a programmable quantum simulator. *Science* **2021**, *374*, 1242–1247. [\[CrossRef\]](#)
- Bravyi, S.; Gambetta, J.M.; Mezzacapo, A.; Temme, K. Tapering off qubits to simulate fermionic Hamiltonians. *arXiv* **2017**, arXiv:1701.08213.
- Setia, K.; Chen, R.; Rice, J.E.; Mezzacapo, A.; Pistoia, M.; Whitfield, J.D. Reducing Qubit Requirements for Quantum Simulations Using Molecular Point Group Symmetries. *J. Chem. Theory Comput.* **2020**, *16*, 6091–6097. [\[CrossRef\]](#) [\[PubMed\]](#)
- Faist, P.; Nezami, S.; Albert, V.V.; Salton, G.; Pastawski, F.; Hayden, P.; Preskill, J. Continuous symmetries and approximate quantum error correction. *Phys. Rev. X* **2020**, *10*, 041018. [\[CrossRef\]](#)

24. Elfving, V.E.; Millaruelo, M.; Gámez, J.A.; Gogolin, C. Simulating quantum chemistry in the seniority-zero space on qubit-based quantum computers. *Phys. Rev. A* **2021**, *103*, 032605. [[CrossRef](#)]
25. Eddins, A.; Motta, M.; Gujarati, T.P.; Bravyi, S.; Mezzacapo, A.; Hadfield, C.; Sheldon, S. Doubling the Size of Quantum Simulators by Entanglement Forging. *PRX Quantum* **2022**, *3*, 010309. [[CrossRef](#)]
26. Gard, B.T.; Zhu, L.; Barron, G.S.; Mayhall, N.J.; Economou, S.E.; Barnes, E. Efficient symmetry-preserving state preparation circuits for the variational quantum eigensolver algorithm. *npj Quantum Inf.* **2020**, *6*, 1–9. [[CrossRef](#)]
27. Kuroiwa, K.; Nakagawa, Y.O. Penalty methods for a variational quantum eigensolver. *Phys. Rev. Res.* **2021**, *3*, 013197. [[CrossRef](#)]
28. Logemann, R.; Rudenko, A.; Katsnelson, M.; Kirilyuk, A. Exchange interactions in transition metal oxides: The role of oxygen spin polarization. *J. Phys. Cond. Mat.* **2017**, *29*, 335801. [[CrossRef](#)]
29. Schurkus, H.F.; Chen, D.; O'Rourke, M.J.; Cheng, H.P.; Chan, G.K.L. Exploring the Magnetic Properties of the Largest Single-Molecule Magnets. *J. Phys. Chem. Lett.* **2020**, *11*, 3789–3795. [[CrossRef](#)]
30. Sugisaki, K.; Nakazawa, S.; Toyota, K.; Sato, K.; Shiomi, D.; Takui, T. Quantum chemistry on quantum computers: A method for preparation of multiconfigurational wave functions on quantum computers without performing post-Hartree–Fock calculations. *ACS Cent. Sci.* **2018**, *5*, 167–175. [[CrossRef](#)]
31. Rost, B.; Jones, B.; Vyushkova, M.; Ali, A.; Cullip, C.; Vyushkov, A.; Nabrzyski, J. Simulation of Thermal Relaxation in Spin Chemistry Systems on a Quantum Computer Using Inherent Qubit Decoherence. *arXiv* **2020**, arXiv:2001.00794.
32. Jones, J.A.; Hore, P.J. Spin-selective reactions of radical pairs act as quantum measurements. *Chem. Phys. Lett.* **2010**, *488*, 90–93. [[CrossRef](#)]
33. Cao, Y.; Romero, J.; Olson, J.P.; Degroote, M.; Johnson, P.D.; Kieferová, M.; Kivlichan, I.D.; Menke, T.; Peropadre, B.; Sawaya, N.P.; et al. Quantum chemistry in the age of quantum computing. *Chem. Rev.* **2019**, *119*, 10856–10915. [[CrossRef](#)] [[PubMed](#)]
34. Motta, M.; Rice, J.E. Emerging quantum computing algorithms for quantum chemistry. *WIREs Comput. Mol. Sci.* **2021**, e1580. [[CrossRef](#)]
35. Bacon, D.; Chuang, I.L.; Harrow, A.W. Efficient quantum circuits for Schur and Clebsch–Gordan transforms. *Phys. Rev. Lett.* **2006**, *97*, 170502. [[CrossRef](#)]
36. Sugisaki, K.; Yamamoto, S.; Nakazawa, S.; Toyota, K.; Sato, K.; Shiomi, D.; Takui, T. Open shell electronic state calculations on quantum computers: A quantum circuit for the preparation of configuration state functions based on Serber construction. *Chem. Phys. Lett. X* **2019**, *1*, 100002. [[CrossRef](#)]
37. Bärttschi, A.; Eidenbenz, S. Deterministic preparation of Dicke states. In *Fundamentals of Computation Theory*; Gasieniec, L.A., Jansson, J., Levcopoulos, C., Eds.; Springer: Berlin, Germany, 2019; pp. 126–139.
38. Barenco, A.; Bennett, C.H.; Cleve, R.; DiVincenzo, D.P.; Margolus, N.; Shor, P.; Sleator, T.; Smolin, J.A.; Weinfurter, H. Elementary gates for quantum computation. *Phys. Rev. A* **1995**, *52*, 3457. [[CrossRef](#)]
39. Cerezo, M.; Arrasmith, A.; Babbush, R.; Benjamin, S.C.; Endo, S.; Fujii, K.; McClean, J.R.; Mitarai, K.; Yuan, X.; Cincio, L.; et al. Variational quantum algorithms. *Nat. Rev. Phys.* **2021**, *3*, 625–644. [[CrossRef](#)]
40. Peruzzo, A.; McClean, J.; Shadbolt, P.; Yung, M.H.; Zhou, X.Q.; Love, P.J.; Aspuru-Guzik, A.; O'Brien, J.L. A variational eigenvalue solver on a photonic quantum processor. *Nat. Commun.* **2014**, *5*, 4213. [[CrossRef](#)]
41. McClean, J.R.; Romero, J.; Babbush, R.; Aspuru-Guzik, A. The theory of variational hybrid quantum-classical algorithms. *New J. Phys.* **2016**, *18*, 023023. [[CrossRef](#)]
42. Parrish, R.M.; Hohenstein, E.G.; McMahon, P.L.; Martinez, T.J. Hybrid quantum/classical derivative theory: Analytical gradients and excited-state dynamics for the multistate contracted variational quantum eigensolver. *arXiv* **2019**, arXiv:1906.08728.
43. Schuld, M.; Bergholm, V.; Gogolin, C.; Izaac, J.; Killoran, N. Evaluating analytic gradients on quantum hardware. *Phys. Rev. A* **2019**, *99*, 032331. [[CrossRef](#)]
44. Mitarai, K.; Nakagawa, Y.O.; Mizukami, W. Theory of analytical energy derivatives for the variational quantum eigensolver. *Phys. Rev. Res.* **2020**, *2*, 013129. [[CrossRef](#)]
45. Kottmann, J.S.; Anand, A.; Aspuru-Guzik, A. A feasible approach for automatically differentiable unitary coupled-cluster on quantum computers. *Chem. Sci.* **2021**, *12*, 3497–3508. [[CrossRef](#)]
46. Kandala, A.; Mezzacapo, A.; Temme, K.; Takita, M.; Brink, M.; Chow, J.M.; Gambetta, J.M. Hardware-efficient variational quantum eigensolver for small molecules and quantum magnets. *Nature* **2017**, *549*, 242–246. [[CrossRef](#)] [[PubMed](#)]
47. Sharma, A.; Tulapurkar, A.A. Preparation of spin eigenstates including the Dicke states with generalized all-coupled interaction in a spintronic quantum computing architecture. *Quantum Inf. Process.* **2021**, *20*, 1–26. [[CrossRef](#)]
48. Farhi, E.; Goldstone, J.; Gutmann, S. A quantum approximate optimization algorithm. *arXiv* **2014**, arXiv:1411.4028.
49. Trotter, H.F. On the product of semi-groups of operators. *Proc. AMS* **1959**, *10*, 545–551. [[CrossRef](#)]
50. Suzuki, M. Generalized Trotter's formula and systematic approximants of exponential operators and inner derivations with applications to many-body problems. *Comm. Math. Phys.* **1976**, *51*, 183–190. [[CrossRef](#)]
51. Childs, A.M.; Su, Y.; Tran, M.C.; Wiebe, N.; Zhu, S. Theory of Trotter Error with Commutator Scaling. *Phys. Rev. X* **2021**, *11*, 011020. [[CrossRef](#)]
52. Childs, A.M.; Su, Y. Nearly Optimal Lattice Simulation by Product Formulas. *Phys. Rev. Lett.* **2019**, *123*, 050503–050509. [[CrossRef](#)] [[PubMed](#)]
53. Aleksandrowicz, G.; Alexander, T.; Barkoutsos, P.; Bello, L.; Ben-Haim, Y.; Bucher, D.; Cabrera-Hernández, F.; Carballo-Franquis, J.; Chen, A.; Chen, C.; et al. Qiskit: An open-source framework for quantum computing. *Zenodo* **2019**, *16*. [[CrossRef](#)]

54. Kingma, D.P.; Ba, J. Adam: A method for stochastic optimization. *arXiv* **2014**, arXiv:1412.6980.
55. Stokes, J.; Izaac, J.; Killoran, N.; Carleo, G. Quantum natural gradient. *Quantum* **2020**, *4*, 269. [[CrossRef](#)]
56. Spall, J.C. An overview of the simultaneous perturbation method for efficient optimization. *Johns Hopkins APL Tech. Dig.* **1998**, *19*, 482–492.
57. Spall, J.C. Adaptive stochastic approximation by the simultaneous perturbation method. *Proc. IEEE Conf. Decis. Control* **1998**, *4*, 3872–3879. [[CrossRef](#)]
58. Bhatnagar, S.; Prasad, H.; Prashanth, L. *Stochastic Recursive Algorithms for Optimization: Simultaneous Perturbation Methods*; Springer: Berlin, Germany, 2013.
59. Hestenes, M.R.; Stiefel, E. *Methods of Conjugate Gradients for Solving Linear Systems*; NBS: Washington, DC, USA, 1952; Volume 49.
60. Cross, A.W.; Bishop, L.S.; Sheldon, S.; Nation, P.D.; Gambetta, J.M. Validating quantum computers using randomized model circuits. *Phys. Rev. A* **2019**, *100*, 032328. [[CrossRef](#)]
61. *ibmq\_athens* v1.3.1, *ibmq\_santiago* v1.2.1, and *ibmq\_manila* v1.1.1. IBM Quantum Team. 2020. Available online: <https://quantum-computing.ibm.com> (accessed on 1 February 2022).
62. Temme, K.; Bravyi, S.; Gambetta, J.M. Error mitigation for short-depth quantum circuits. *Phys. Rev. Lett.* **2017**, *119*, 180509. [[CrossRef](#)]
63. Kandala, A.; Temme, K.; Córcoles, A.D.; Mezzacapo, A.; Chow, J.M.; Gambetta, J.M. Error mitigation extends the computational reach of a noisy quantum processor. *Nature* **2019**, *567*, 491–495. [[CrossRef](#)]
64. Bravyi, S.; Sheldon, S.; Kandala, A.; Mckay, D.C.; Gambetta, J.M. Mitigating measurement errors in multi-qubit experiments. *arXiv* **2020**, arXiv:2006.14044.
65. Maciejewski, F.B.; Zimborás, Z.; Oszmaniec, M. Mitigation of readout noise in near-term quantum devices by classical post-processing based on detector tomography. *Quantum* **2020**, *4*, 257. [[CrossRef](#)]
66. Dumitrescu, E.F.; McCaskey, A.J.; Hagen, G.; Jansen, G.R.; Morris, T.D.; Papenbrock, T.; Pooser, R.C.; Dean, D.J.; Lougovski, P. Cloud Quantum Computing of an Atomic Nucleus. *Phys. Rev. Lett.* **2018**, *120*, 210501. [[CrossRef](#)]
67. Stamatopoulos, N.; Egger, D.J.; Sun, Y.; Zoufal, C.; Iten, R.; Shen, N.; Woerner, S. Option pricing using quantum computers. *Quantum* **2020**, *4*, 291. [[CrossRef](#)]
68. Samach, G.O.; Greene, A.; Borregaard, J.; Christandl, M.; Kim, D.K.; McNally, C.M.; Melville, A.; Niedzielski, B.M.; Sung, Y.; Rosenberg, D.; et al. Lindblad Tomography of a Superconducting Quantum Processor. *arXiv* **2021**, arXiv:2105.02338.
69. Dicke, R.H. Coherence in spontaneous radiation processes. *Phys. Rev.* **1954**, *93*, 99. [[CrossRef](#)]
70. Prevedel, R.; Cronenberg, G.; Tame, M.S.; Paternostro, M.; Walther, P.; Kim, M.S.; Zeilinger, A. Experimental realization of Dicke states of up to six qubits for multiparty quantum networking. *Phys. Rev. Lett.* **2009**, *103*, 020503. [[CrossRef](#)]
71. Özdemir, S.K.; Shimamura, J.; Imoto, N. A necessary and sufficient condition to play games in quantum mechanical settings. *New J. Phys.* **2007**, *9*, 43. [[CrossRef](#)]
72. Tóth, G. Multipartite entanglement and high-precision metrology. *Phys. Rev. A* **2012**, *85*, 022322. [[CrossRef](#)]
73. Childs, A.M.; Farhi, E.; Goldstone, J.; Gutmann, S. Finding Cliques by Quantum Adiabatic Evolution. *Quant. Info. Comput.* **2002**, *2*, 181–191. [[CrossRef](#)]